

Article

Application of Nondestructive Techniques to Investigate Dissolvable Amorphous Metal Tungsten Nitride for Transient Electronics and Devices

Abdulilah Mohammad Mayet ^{1,*}, Mohammed Abdul Muqet ¹, Ali Awadh Alqahtani ¹, Muhammad Abbas Khan ², Abdulrahim Othman Dawbi ¹, Hala H. Alhashim ³, Ramy Mohammed Aiesh Qaisi ⁴, Nivin A. Ghamry ⁵ and Elsayed M. Tag-Eldin ^{6,*}

¹ Electrical Engineering Department, College of Engineering, King Khalid University, Abha 61421, Saudi Arabia

² Department of Electrical Engineering, Balochistan University of Information Technology, Engineering and Management Sciences, Quetta 87300, Pakistan

³ Department of Physics, College of Science, Imam Abdulrahman Bin Faisal University, Dammam 31441, Saudi Arabia

⁴ Department of Electrical and Electronics Engineering, College of Engineering, University of Jeddah, Jeddah 21589, Saudi Arabia

⁵ Faculty of Computers and Artificial Intelligene, Cairo University, Giza 3387722, Egypt

⁶ Electrical Engineering Department, Faculty of Engineering, Technology, Future University in Egypt, New Cairo 11835, Egypt

* Correspondence: amayet@kku.edu.sa (A.M.M.); elsayed.tageldin@fue.edu.eg (E.M.T.-E.)



Citation: Mayet, A.M.; Muqet, M.A.; Alqahtani, A.A.; Khan, M.A.; Dawbi, A.O.; Alhashim, H.H.; Qaisi, R.M.A.; Ghamry, N.A.; Tag-Eldin, E.M. Application of Nondestructive Techniques to Investigate Dissolvable Amorphous Metal Tungsten Nitride for Transient Electronics and Devices. *Electronics* **2022**, *11*, 3284. <https://doi.org/10.3390/electronics11203284>

Academic Editor: Gholam Hossein Roshani

Received: 20 September 2022

Accepted: 9 October 2022

Published: 12 October 2022

Publisher's Note: MDPI stays neutral with regard to jurisdictional claims in published maps and institutional affiliations.



Copyright: © 2022 by the authors. Licensee MDPI, Basel, Switzerland. This article is an open access article distributed under the terms and conditions of the Creative Commons Attribution (CC BY) license (<https://creativecommons.org/licenses/by/4.0/>).

Abstract: Transient electronics can be gradually dissolved in a variety of liquids over time. The short-lived nature of such electronics has promoted their implementation in prospective applications, such as implantable electronics, dissolvable devices for secure systems, and environmentally biodegradable electronics. The amorphous metal tungsten nitride (WN_x) has the remarkable ability to scale down to the nano-scale, allowing the fabrication of sub-1 volt nano-electromechanical (NEM) switches. When compared to silicon, amorphous WN_x has a greater density and electrical conductivity, making it an even more appealing material for the design of accelerometers and resistive temperature detectors. Kinetic hydrolysis is observed by the dissolution of amorphous WN_x in ground water. To better understand the kinetics of hydrolysis, in this paper, samples are dissolved in different solutions under different conditions over time. NEM switches immersed in ground water, de-ionized (DI) water, and salty water are subjected to temperatures of 0 °C (degrees Celsius), 25 °C (room temperature, RT), and 60 °C. Sonicated samples are tested at both room temperature (RT) and at 60 °C. During the course of dissolving, the resistivity of amorphous WN_x is measured, and an increase in resistance is noted when the thickness of the amorphous WN_x is reduced. The wettability of a solid can be easily determined by measuring its contact angle, which indicates either the hydrophobic or hydrophilic nature of the surface. The contact angle of the amorphous WN_x is measured to be about 30.8°, indicating hydrophilicity. For the temperature sensor characterization, a probe station with a thermal chuck is used to apply heat from the bottom of the sensor. The actual real-time temperature of the amorphous WN_x sensor is measured using a thermocouple tip on the surface of the sensor.

Keywords: dissolution; sonication; accelerometer; resistive temperature detector; wettability; nondestructive technique; solubility

1. Introduction

Amorphous WN_x has the remarkable ability to scale down to the nano-scale, which is necessary for the fabrication of sub-1 volt NEM switches [1]. When the moving electromechanical component of NEM switches is scaled down, the resulting switch often has poor mechanical qualities [2–4]. These features include wear, aggravation, fracture, fatigue, and electrical discharge surface damage. These mechanical obstacles may be reduced to a

minimum if the NEM switches are fabricated using amorphous WN_x . Because tungsten naturally contains nitrogen atoms, the synthesis of native oxide is inhibited to a significant degree [5].

Recently, researchers have demonstrated significant advances in dissolvable electronics [6–9]. Their categorical studies have shown that a broad class of inorganic and organic dissolvable materials exists in nature, including silk, silicon, silicon germanium (SiGe), indium gallium zinc oxide (IGZO), molybdenum (Mo), iron (Fe), tungsten (W), zinc (Zn) foils, magnesium (Mg), Mg alloys, metastable poly phthalaldehyde, carbon nanotubes (CNTs), polylactic-co-glycolic acid (PLGA), the copolymer of poly lactic acid (PLA), poly glycolic acid (PGA), polycaprolactone (PCL), and rice paper. Nevertheless, all the metals used in the corresponding reports are poly-crystalline [10]. Unfortunately, for nano-scale devices, especially harsh environment compatible nano-electromechanical systems (NEMSs), such poly-crystalline metals present limitations due to their large grain size, rendering them impractical [11–13]. It is nearly impossible to form a uniformly shaped and sized nano-scale device with such crystalline materials. In fact, during material patterning, i.e., etching, the irregular grain size significantly deforms the architecture and causes unwanted non-uniformities in device characteristics [8]. Due to the lack of considerably bigger grains and related barriers during subtractive etching, an amorphous metal may be a viable solution to nano-scale devices and systems.

The miniaturization of micro-electromechanical switch (MEMS) accelerometers results in smaller components and packages, which ultimately leads to a lower cost and sensitivity. This is essential for emerging applications, such as wearable electronics, biomedical implants, nano-scale robotics, and the internet of things (IoT), all of which are becoming increasingly important. Miniaturizing the electromechanical transducer and reducing the size of the proof mass are two components of the downscaling process for MEMS accelerometers [14]. Accelerometers and gyroscopes made using NEMS technology often need masses to be fastened to membranes, beams, or cantilevers that are hung in space. Piezoresistive electromechanical transducers made out of graphene ribbons with suspended silicon proof masses have been used in NEMS accelerometers with direct electrical readouts. Applications where low-cost accelerometers are desirable include hard-drive security; mobile device motion interfaces; and video games, motion capture, and control systems that use gesture recognition [15–17].

Nanomechanical sensors have a wide variety of biological applications, ranging from physiological parameter monitoring to bioinformatics. Nanomechanical sensors, which operate on micro- and nano-scales, can detect and identify the existence of biological entities at very low concentrations based on their mass and mechanical characteristics, and they can describe the motion and forces associated with biomolecular activities. There are a variety of distinct detecting concepts that underpin each mode of operation. One kind of temperature sensor is a resistance temperature detector, or RTD. RTDs are temperature sensors that may be used between $-200\text{ }^{\circ}\text{C}$ and $+850\text{ }^{\circ}\text{C}$, and they have a consistent resistance vs. temperature relationship regardless of the material they are made from. Resistance temperature detectors (RTDs) have a thermostat whose resistance value varies in response to changes in the device's temperature [18,19].

Metal refining and energy generation rely heavily on dissolution processes. The synthesis of a mixture is an illustration of a spontaneous process, which happens under specific circumstances without the need for energy from an external source. One may often agitate a combination to speed up the dissolving process, although this is not essential; if one waits long enough, a homogenous solution will emerge. Internal energy changes often occur, but not always, throughout the dissolution process when heat is absorbed or evolved. In the metallurgical process of electro-polishing and anisotropic etching, as well as digesting, they play an essential role. Furthermore, they have always had a close relationship with cathodic processes, such as electro-deposition [20]. Since the anodic reaction in metal deposition involves the breakdown of water, which is often quicker than the electro-deposition process, it is typically neglected. Passive film development

is a frequent problem in aqueous solutions, and a dimensionally stable anode is needed. Typical solvents are ineffective against metals in their elemental form. In order for them to be dissolved, an oxidation process must take place concurrently [8,20]. An oxidizing agent (to oxidize the metal), a solvent (water or a non-aqueous solvent) to dissolve the oxidizing agent, and, in some cases, a compelling agent to modify the metals' redox potential and/or the solubility of the produced metal compounds are all necessary for the oxidative dissolution of metals [8–10,21,22]. Applications where the oxidative dissolution of metallic components is necessary include chemical etching in the microelectronics sector, the surface polishing of metals or alloys, and the extraction of gold from gold-bearing ores.

The capacity of a liquid to interact with another liquid or a solid surface is referred to as its "wettability". That is, the degree to which a solid and a liquid phase interact is quantified by a property called "wettability" [23,24]. Measurements of the contact angle between a surface and a liquid are the most frequent method used to determine the wettability of polymeric biomaterials [25]. Wetting ability is directly related to oxygen incorporation, which, in turn, affects cell adhesion. Platelets adhere better to hydrophobic surfaces than they do to hydrophilic ones [5,23,24]. Tungsten nitride (WN_x) is an amorphous metal with a grainless molecular structure, and its solubility and biocompatibility are the subjects of this study. The structure of tungsten nitride makes it resistant to corrosion, provides extreme durability and a smooth surface, and results in minimal contact wear and aggravation.

2. Experimental Methods and Discussion

The fabrication process starts by sputtering amorphous WN_x on the demanded substrate, either a silicon wafer for micromachining or an arbitrary substrate for a certain functional device. The wafer is first cleaned in sonicated baths of acetone, iso-propanol, and deionized water. Using plasma-enhanced chemical vapor deposition (PECVD), Silicon Dioxide (SiO_2) is deposited at 300 °C and 1 Torr under a Silane (SiH_4), Nitrous Oxide (N_2O), and nitrogen (N_2) plasma to create a sacrificial and isolating layer of 2 μm in thickness. With a tungsten target and 5 millitorr (mTorr) of pressure, 100 nano-meters (nm) of amorphous WN_x is deposited through reactive ion sputtering. The tungsten target is then exposed to a combination of argon (35 sccm) and nitrogen (5 sccm) gas, which react to produce amorphous WN_x . Next, 300 nm of SiO_2 is deposited on top of the amorphous tungsten nitride (αWN_x) to be used as a hard mask for patterning and micromachining the WN_x . The hard mask is patterned using the negative e-beam resist for the NEM switch, and using a contact aligner in the case of the accelerometer, and subsequently etched with reactive ion etching, using C_4F_8 and O_2 plasma at 10 °C and 10 mTorr pressure. The amorphous metal tungsten nitride (αWN_x) layer is etched using Cl_2 and O_2 plasma at 80 °C and 5 mTorr pressure. The sacrificial layer is etched using Hydrogen Fluoride (HF) vapor to obtain the freestanding (stand-alone) structure. In the case of an arbitrary insulating substrate, neither SiO_2 nor the micromachining step is needed. The structured pattern is obtained by placing a carved shadow mask patterned with the desired design on top of an arbitrary substrate during the sputtering process of amorphous WN_x . This method is more convenient for the fabrication of large-sized structures over 500 micro-meters (μm), such as heaters and temperature sensors.

Amorphous WN_x thin film is prepared through the reactive sputtering deposition technique, using tungsten (W) and a combination of argon (Ar) and nitrogen (N_2) gases. WN_x -based devices can be fabricated using two different process integration sequences (Figure 1): (i) a lithography-based patterning process (Figure 1a–d), mainly for micro- and nano-scale device dimensions, or (ii) a shadow-mask-assisted technique, for the design of macro-scale-level patterns (Figure 1e,f). For the lithography-based process, we deposit a Silicon Dioxide (SiO_2) layer on top of a silicon (Si) wafer using the plasma-enhanced chemical vapor deposition (PECVD) process (Figure 1a). Silicon Dioxide served as both an electrical insulator and a sacrificial layer. Thin amorphous WN_x is then sputter-deposited as the metal conductor (Figure 1b), and reactive ion etching (RIE) is used to pattern the desired device architecture (Figure 1c). Moreover, this technique is used to fabricate accelerometers

and nano- and micro-electromechanical systems (NEMSs and MEMSs). Nano-scale NEM switches are built using electron beam lithography (EBL) and the patterning process, as shown in Figure 1c. A cavity is then formed by selectively etching away the sacrificial SiO_2 using vapor hydrofluoric acid (VHF), as shown in Figure 1d. This is an essential step in the construction of a free-moving NEMS and/or MEMS switch.

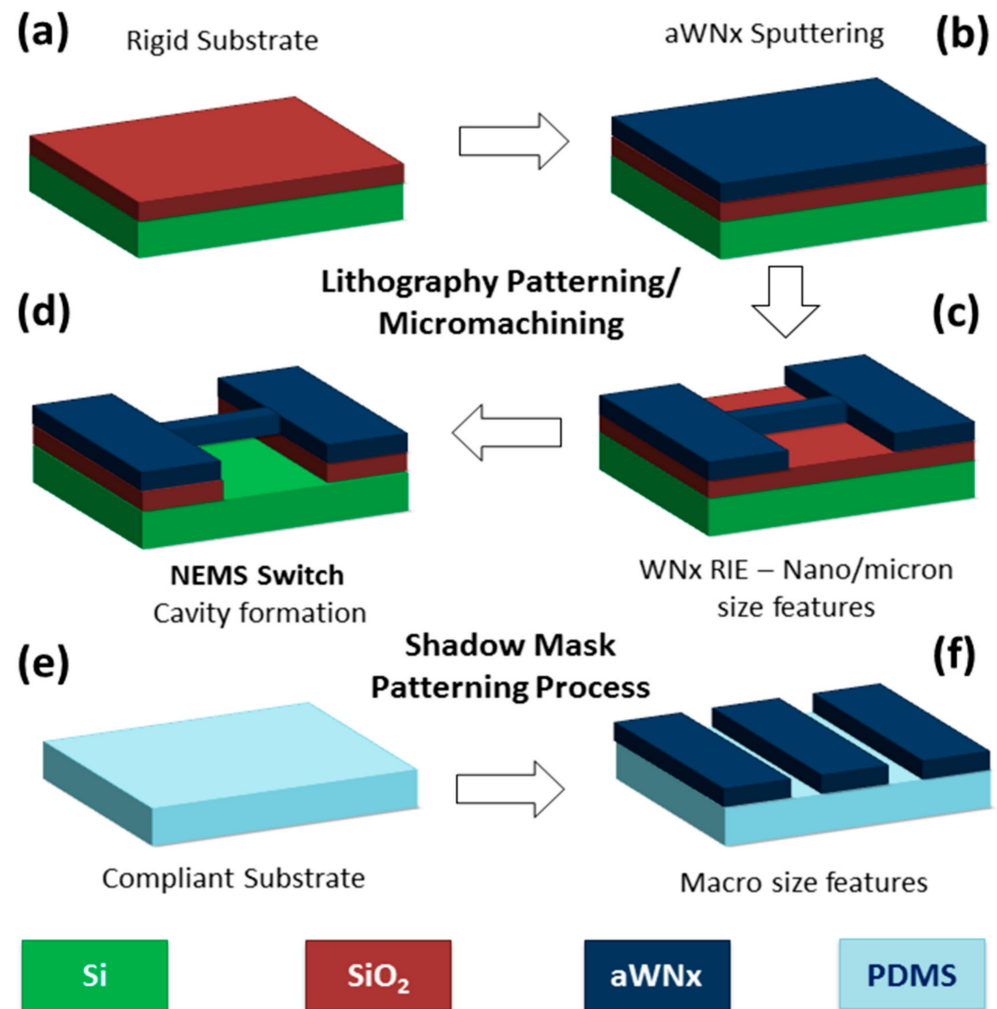


Figure 1. Two process integration sequences for amorphous WN_x -based devices. (a) Micromachining method for small-feature-size devices starting with a rigid Si substrate with an oxide layer deposited on top using PECVD; (b) 100 nm amorphous WN_x deposition through sputtering technique; (c) micro-/nano-feature patterning through lithography and RIE; (d) cavity formation by partially releasing SiO_2 sacrificial layer to form the final NEMS switch structure; (e) schematic of the shadow mask method for large structures and macro-sized features starting with a compliant PDMS substrate; (f) formation of desired patterns through lift-off of deposited WN_x film.

Figure 2a shows the design layout of the NEM device, along with a scanning electron microscope (SEM) image (**Inset S1**) and an electrical characteristics plot displaying the drive current vs. gate voltage performance (**Inset S2**). As previously discussed, amorphous WN_x has the unique property of scaling down to nano-scale in order to fabricate sub-1 volt NEM switches. Fabricating NEM switches using amorphous WN_x minimizes the mechanical hindrances. Native oxide formation is minimized due to the existence of nitrogen atoms in tungsten. These properties, besides the high density of amorphous WN_x ($\rho_c = 17 \text{ g}\cdot\text{cm}^{-3}$), give superiority to amorphous WN_x for the fabrication of nano-scale devices. The transfer (I - V) characteristic of the device is determined using a Keithley

4200 SCS parameter analyzer. The source of the device (the cantilever) is grounded, while the gate voltage is swept from 0 to 10 V in steps of 50 mV. Figure 2a also shows a NEM switch fully operational after the release step, with a 100 nm thickness and a length of a few microns, exhibiting a pull-in voltage of less than 2 V. The design device also surpasses multiple runs with no deterioration in I–V characteristics. The most important parameter of a NEM switch is its pull-in voltage, i.e., the voltage at which the cantilever is drawn toward the gate, establishing contact with the source. The pull-in voltage can be theoretically calculated using Equation (1) for a two-terminal vertical NEM switch [1]:

$$V_{pi} = \sqrt{\frac{2Ed^3t^3}{27\epsilon_0L_C^4}} \tag{1}$$

where E is the Young’s modulus of WN_x , d is the air gap between the gate electrode and the cantilever, L_C is the cantilever length, t is the thickness of the cantilever, and ϵ_0 is the permittivity of air.

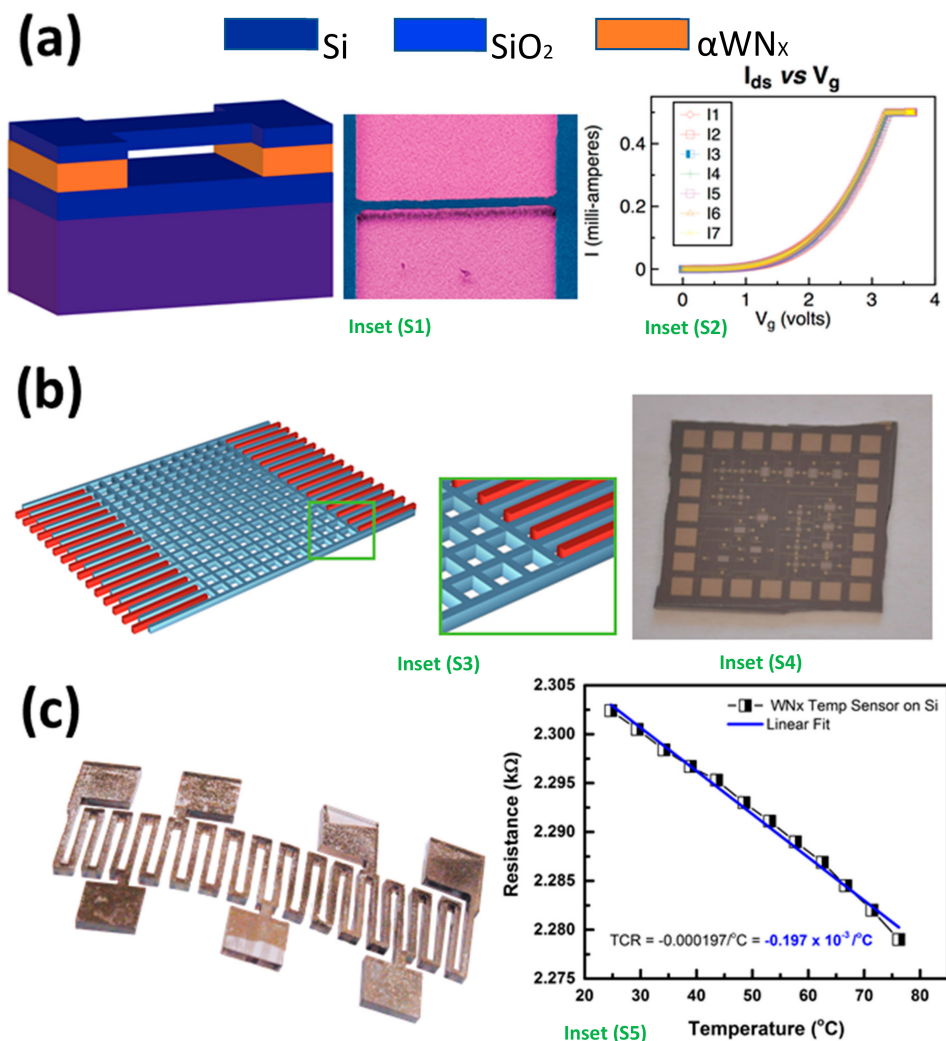


Figure 2. WN_x -based devices. (a) Schematic of nano-scale NEM switch design layout, the corresponding SEM image (Inset S1), and the I–V characteristics plot (Inset S2); (b) micro-scale accelerometer design layout (rivet snippet shown in Inset S3) and optical image of the fabricated device (Inset S4); (c) a macro-scale resistive temperature sensor design layout, with the corresponding sensitivity plot (Inset S5).

Amorphous-WN_x-based accelerometers are built using the lithography-based fabrication process. In this case, the amorphous WN_x layer is micro-machined using a generic contact aligner to pattern the desired microstructure. Figure 2b shows the design layout (rivet image showed in Inset S3) and an optical image of the fabricated accelerometers (Inset S4). In general, amorphous WN_x exhibits a higher density and electrical conductivity than silicon, making it an even more attractive material for accelerometers. To produce a differential capacitor for a surface micro-machined capacitive accelerometer, the fixed plates on the wafer are driven 180° out of phase from the fixed plates on the mass and the base substrate. If the mass is moved, the capacitor is flung out of balance and produces a square wave whose amplitude is proportional to the acceleration. Despite the micro-scale structure of the accelerometer, the high hardness (3 GPa) and Young's modulus (300 GPa) of amorphous WN_x allow us to fabricate long-facing electrodes, yielding a capacitance magnitude of 30 ± 10 pF for the maximum travel of proof mass in both directions, measured using an LCR meter. A demodulator is used for each axis to determine the direction of acceleration. Based on this, materials with a heavy proof mass, such as silicon, have been adopted to optimize the performance of accelerometers. Nevertheless, WN_x displays an even higher density, which corresponds to a heavier proof mass, and a higher conductivity leading to a higher resonant frequency, consequently enhancing the quality factor and optimizing the performance of capacitive accelerometers, as stated in Equations (2) and (3) for the resonant frequency of spring-mass structures [26]:

$$Q = \frac{2\pi f_0 m}{b} \quad (2)$$

$$f_0 = \frac{2}{\pi} \sqrt{\frac{wt^3 E}{mL}} \quad (3)$$

where f_0 is the resonant frequency, m is the mass, b is the damping coefficient, w is the width of the spring, t is the thickness of the spring, and L is the length of the spring.

Finally, a millimeter-sized resistive temperature detector (RTD) is fabricated to demonstrate the efficient dissolution of large surface areas. In this case, we resort to the shadow mask patterning process. We start with an arbitrary flexible substrate, such as polydimethylsiloxane (PDMS) (Figure 1e), onto which we place a shadow mask patterned with the desired resistive structure (Figure 2c–Inset S5). Amorphous WN_x is then sputtered, using the shadow mask to reveal the fully functional temperature sensors. This technique simplifies the fabrication of large structures using a single step, without resorting to complex micromachining.

Amorphous WN_x has a high electrical conductivity of $5.0 \times 10^6 \mu\text{S}\cdot\text{cm}$, making it a good candidate for resistive-based temperature-sensing materials. The characterization of the sensor was performed on a thermal chuck, where the temperature was varied from 25 °C to 75 °C in steps of 5 °C. Regarding the accuracy of the measurements, the real temperature observed by the sensor was measured using a surface-mounted thermocouple on the WN_x film. The resistance of the sensor was measured using a digital source meter through a 4-point probe measurement technique. Usually, in RTDs, when metal films are exposed to elevated temperatures, phonon vibrations occur in the lattice structure of the material, leading to more collisions and, hence, an increase in resistance. In contrast, when using a semiconductor, an insulating film, or an alloy, higher temperatures lead to a decrease in the resistance of the film. In fact, for this set of materials, at lower temperatures, electrons are trapped within the atom. When exposed to higher temperatures, electrons are energized, gaining enough energy to escape from the confinement of their atoms. That is, electrons gain sufficient kinetic energy to jump from the valence band to the conduction band. This behavior results in an increase in conductivity, and, hence, a decrease in resistance is

observed. In general, any RTD behavior is illustrated by a linear dependence between resistance and temperature, as depicted in Equation (4):

$$\frac{\Delta R}{R_0} = \alpha \Delta T \quad (4)$$

where R_0 is the initial resistance of the structure (in Ω); ΔR is the change in resistance corresponding to the change in temperature ΔT ; and α (in $1/^\circ\text{C}$) is the temperature coefficient of resistance (TCR) of the sensor, highlighting its sensitivity.

In this case, $\alpha > 0$ for a metal film since there is an increase in resistance, and $\alpha < 0$ for an insulating, semiconductor, or an alloy film due to the decrease in resistance. In this work, we used an alloy film of WN_x for the film material; hence, we expected a decrease in resistance as the temperature increased. This is clearly depicted in Figure 2c, where a linear behavior is shown such that $R = 2314 - 0.4418t$, and there is a TCR of $-0.197 \times 10^3 / ^\circ\text{C}$. The linear change in resistance is quite small, which is consistent with the observed properties of metal nitride alloys that typically provide thermal stability. A 4-point probe measurement technique with a digital source meter was used to collect resistance values through a fixed applied current of 100 A.

Dissolution experiments were conducted on the previously described macro-, micro-, and nano-scale devices (temperature sensors, accelerometers, and NEM switches, respectively). In Figure 3, we see the results of submerging the WN_x temperature sensor on a PDMS substrate under room-temperature ground water, without sonication, for varying amounts of time. It was found that the dissolving process in the experiment of the macro-scale device was more time-consuming than expected, owing to the huge area of dissolution and the penetration of amorphous WN_x in PDMS micro-pores. The adhesion between the amorphous WN_x and the PDMS was observed to be quite strong after this penetration. The dissolution of amorphous WN_x with a 300 nm thickness was time-consuming, taking a total of 36 h. The micro-scale accelerometers were also tested in ground water with dissolution conditions similar to those of the temperature sensor. Figure 3 shows the dissolution states of the devices with time. The corresponding Atomic Force Microscope (AFM) images are also displayed (Figure 3), highlighting the proof mass of the accelerometers. Finally, experiments at the nano-scale level were conducted on the NEM switches. The dissolving process seen in Figure 3 was acquired using a scanning electron microscope (SEM), and it took place at ambient temperature without the use of sonication. The experiments demonstrated that a 300 nm-thick NEM switch dissolves rapidly from both the top and bottom, with the decay being more pronounced at the cantilever's suspended end. The whole gadget vanished after only a day. The amorphous WN_x device sat over a layer of SiO_2 , which was etched, leaving a black residue. Scanning Tunneling Microscopy (STEM) photos of an amorphous WN_x device dissolving in ambient room temperature ground water are displayed in Figure 3. In the first prototype, the thickness of the device was only about 475 nm. Using Platinum/Carbon (Pt/C) deposition as a shield, the STEM specimen was created using an FEI Helios NanoLab 400S FIB/SEM dual beam system. After that, STEM pictures were captured in a High-Angle Annular Dark Field (HAADF), utilizing a 300 kV FEI Titan ST electron microscope. The STEM photos clearly demonstrated the dissolving phenomenon, which included the total loss of the instrument.

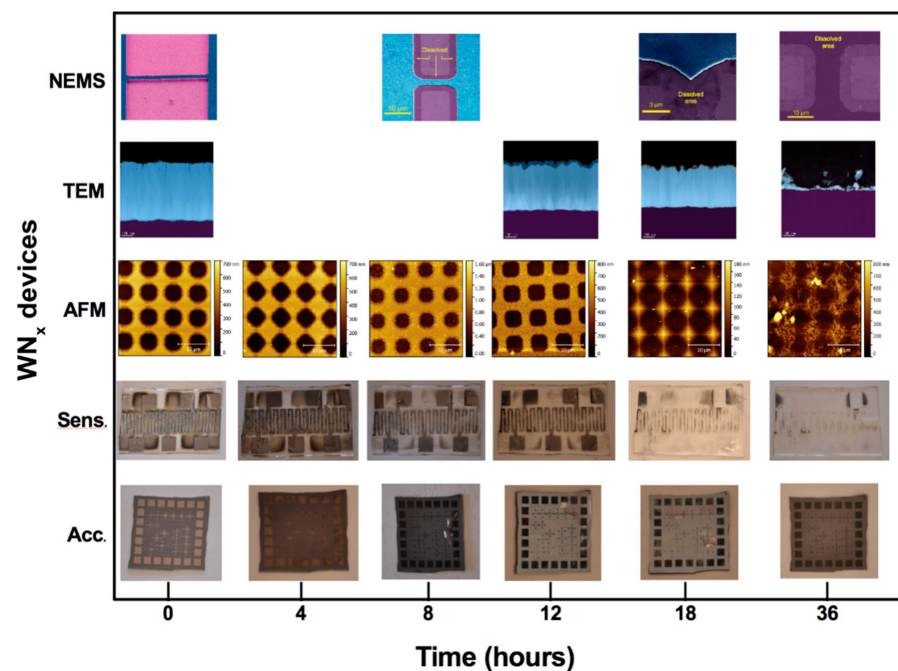
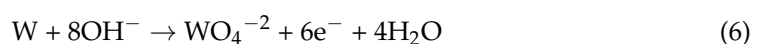


Figure 3. Extensive physical images showing complete dissolution of WN_x devices over time. Devices are submerged in ground water at room temperature, with no sonication.

Assays of WN_x metal solubility were performed by dissolving one sample at a time in 50 mL of the test solution at the specified temperature. After taking the samples out of the solution and washing them in DI water, the authors were able to use a Dektak profile-meter to quantify their thicknesses. The confined solution was analyzed using the instrument Varian 720-ES ICP-Optical Emission Spectrometer to measure the dissolved quantity of tungsten in GW. HeLa cells (ATCC, Manassas, VA, USA) were seeded on both Si and WN_x pieces (1 cm^2) in a Petri dish, with a density of $1 \times 10^6/\text{mL}$, and they were cultured in Eagle's MEM medium (EMEM) (Invitrogen, Carlsbad, CA, USA) containing 10% fetal bovine serum (FBS) (Invitrogen, Carlsbad, CA, USA) and 0.1% penicillin–streptomycin (Invitrogen, Carlsbad, CA, USA) at 37°C in a humidified 5% CO_2 atmosphere for 18 h.

Amorphous WN_x dissolution in ground water indicates the existence of kinetic hydrolysis [10]. The samples were dissolved in a variety of solutions under varying circumstances so that the kinetics of hydrolysis could be studied and understood. Measurements of dissolving behavior were conducted for devices ranging in size from macro-scale sensors to nano-scale NEM switches. To begin, the authors tried experimenting with the NEM switches in a number of different liquids and at a number of different temperatures. Samples sonicated at both room temperature (RT) and 60°C (60°C) were evaluated. Figure 4a–c show the results clearly. It was noted that, at absolute 0°C , the disintegration rate was almost unreal. In addition, this also indicated that ground water is a superior solvent for amorphous WN_x compared to both DI water and salt water. It was hypothesized that the presence of dissolved oxygen initiates the erosion process of amorphous WN_x in water after it has been immersed. The oxygen generates hydroxyl radicals in the presence of free electrons, which dissolve the tungsten in the water by oxidizing the tungsten atoms, as shown in chemical Equations (5) and (6).



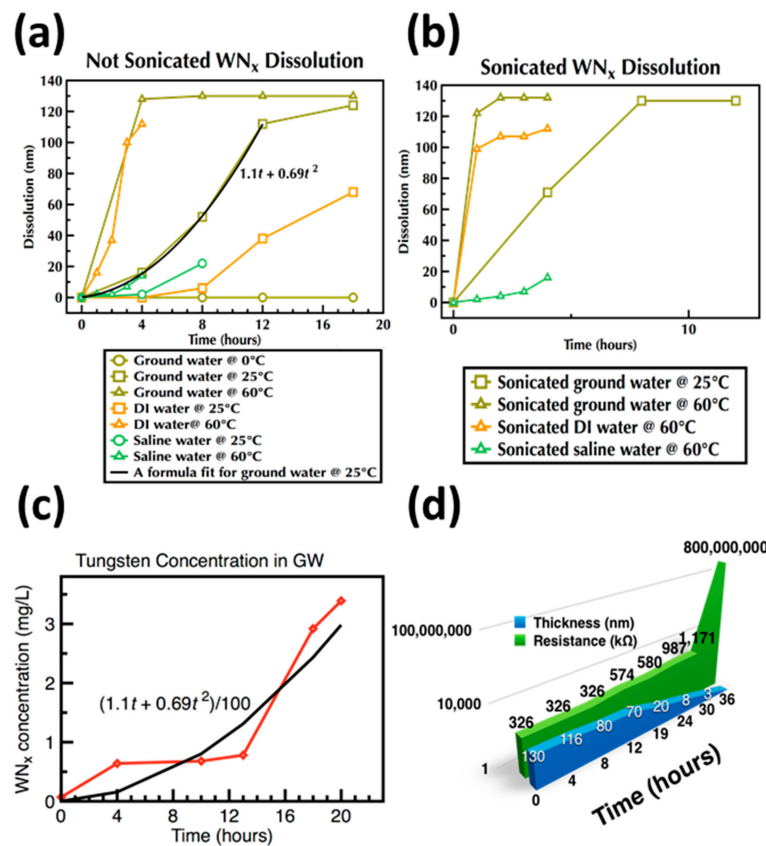


Figure 4. Dissolution rate of amorphous WN_x in different solutions. (a) Dissolution without sonication and (b) dissolution with sonication; (c) tungsten concentration in ground water (GW) solution at RT; (d) relationship between reduction in device thickness over time and resistance.

The complete oxidation reaction generates more free electrons, which, in turn, produce more hydroxyl radicals. A chain reaction starts and rapidly increases the dissolution rate, as indicated in Figure 4a–c. After an appropriate amount of tungsten oxide forms, the corrosion rate (dissolution rate) becomes quick, and the produced device begins rapidly vanishing in comparison to other materials, such as Si and SiO_2 .

Saline water, similar to DI water, has a low dissolving rate because the presence of Na^+ and Cl^- ions limits the quantity of dissolved oxygen in solution and free electrons. In Figure 4a,b, it can be seen that both sonication and heat significantly accelerated the rate of dissolution by elevating the oxidation rate. In a ground water environment, the rate of amorphous WN_x dissolution may be stated as follows:

$$h = 1.1t + 0.69t^2 \tag{7}$$

where h is the dissolved thickness, and t is the time in hours.

During the dissolution process, five samples of ground water at room temperature are measured at different time slots. These samples are analyzed using the instrument Varian 720-ES ICP-Optical Emission Spectrometer to measure the dissolved quantity of tungsten in ground water. The experimental results demonstrate that the dissolution profile is identical to the one expressed in Equation (7); however, as expected, the amplitude is changed due to the different units of measurement and different dissolution conditions, as depicted in Figure 4c and Equation (8). The resistivity of amorphous WN_x is measured during the dissolution process (Figure 4d), and it demonstrates the rise in resistance that occurs when amorphous WN_x is reduced in thickness.

$$h = 0.01 (1.1t + 0.69t^2) \tag{8}$$

From Equations (7) and (8), it is observed that amorphous WN_x has a parabolic dissolution rate against time (Figure 4a–c). This parabolic behavior shows a very low dissolution rate at the beginning, followed by a sudden overshoot. For ground water, it takes around 4 h to speed up the dissolution rate, while it takes only ≈ 8 h for DI water and saline water. Agitation and warming almost double the dissolution rate of amorphous WN_x . Elevated temperatures lead to faster chemical reactions, while sonication breaks intermolecular interactions, hence speeding up the dissolution process. This dissolution behavior is fascinating and demanding for the fabrication of transient electronics, as it signifies that the device could continually operate for a particular time, followed by a process of rapid dissolution. Due to the direct proportionality observed, by adjusting the volumetric size of the amorphous WN_x , we can easily control and manipulate the dissolution time based on thickness.

In order to gain an understanding of the potential amorphous WN_x in vivo applications for implantable transient electronics, human cervical tumor cells, also known as HeLa cells, were allowed to grow for 18 h on both Si and WN_x pieces measuring 1 cm by 1 cm inside a Petri dish. These pieces were sterilized with ultraviolet light and ethanol prior to the experiment. After a lengthy on-chip culture, the cell viability was evaluated using fluorescence labeling in conjunction with a live/dead test (Invitrogen, Carlsbad, CA, USA), which was performed thirty minutes after cell attachment (green: live; red: dead). After that, confocal laser scanning microscopy (CLSM) was utilized to observe the cells in more detail (Zeiss LSM 710 upright confocal microscope). Both (a) silicon and (b) WN_x were shown to support the development and multiplication of cells, as shown in Figure 5a,b, respectively. The amount of living cells, which appear green, and dead cells, which appear red, may be determined using a fluorescent-based live/dead test. It may be deduced that the WN_x surface is less biocompatible than the silicon surface since the cells that were cultivated on silicon adhered and proliferated more than those that were cultured on WN_x . This might be because tungsten and tungsten–metal composites have natural antibacterial characteristics that contribute to their effectiveness. In addition, the wettability of the Si and WN_x surfaces was evaluated using the contact angle (Figure 5c,d).

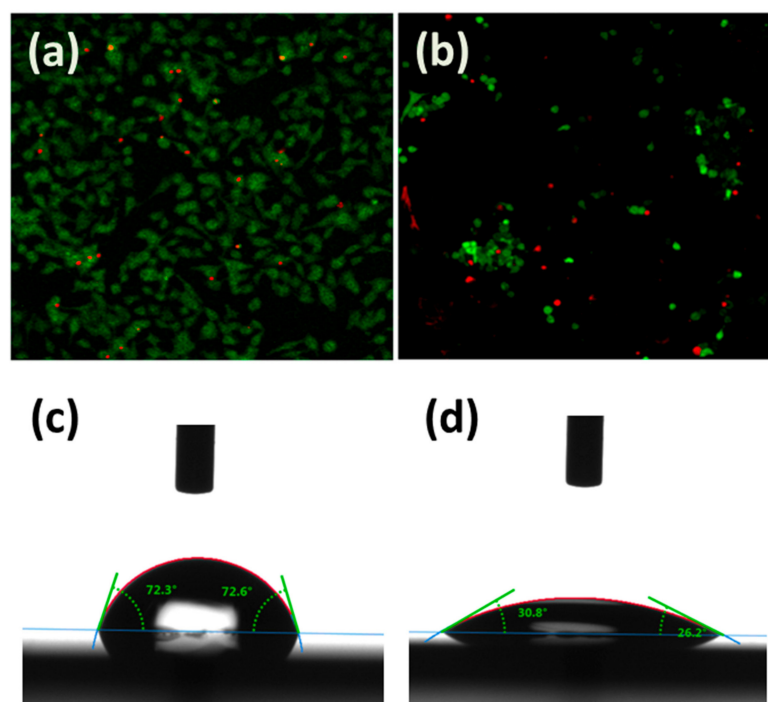


Figure 5. Cells cultured on different materials: (a) on Si; (b) on amorphous WN_x . Contact angle measurements on (c) Si and (d) WN_x surfaces.

3. Conclusions and Future Scope

Transient materials have been proposed for use in valuable applications, ranging from medicine to environmental monitoring, presenting far fewer dangers than non-biodegradable and long-lasting electronics or packaging. We presented a transient amorphous metal, tungsten nitride, and example devices, which were fabricated using industry-standard production techniques. We used proof-of-concept devices, nano-scale (NEMS switches), micro-scale (accelerometers), and macro-scale (millimeter-sized temperature sensors) devices, to test its fabrication ease and potential in dissolvable applications. We found that WN_x offers fast-paced dissolution for in vitro applications. We used an amorphous structure to avoid the performance limitations of polycrystalline forms in nano-scale devices, which are caused by irregularities in grain size that deform device architectures and increase the non-uniformity of device characteristics. We highlighted WN_x 's versatility, as an unprecedented transient material, with average ground water dissolution rates between 20 and 60 nm/h at room temperature. An additional cursory study of the in vivo application of WN_x showed a natural toxicity to HeLa cells compared to a silicon baseline. This may be due to the potential antimicrobial properties of tungsten composites and indicates that, while amorphous tungsten nitride can be dissolved quickly in water, its biocompatibility requires broader study.

According to the findings, ground water is a better candidate for the role of solvent for amorphous WN_x than either DI water or salt water. In spite of the fact that the WN_x surface is more hydrophilic than the Si surface, cells were not able to grow very well on the WN_x surface. This might also be an indication that the products of WN_x dissolution are poisonous to cells, which would make its usage unattractive for implanted biomedical applications, but it would give the possibility of use in dissolvable environmental monitoring sensors. The Internet of Everything requires environmentally sustainable and physiologically safe forms of future electronics that may be briefly utilized while preserving their dependability. These forms must also be adaptable. We showed WN_x to be an amorphous material that is completely dissolvable, and we manufactured electromechanical devices that span a range of sizes in order to emphasize the capabilities of this material in the context of the area of transient electronics.

Author Contributions: Conceptualization, A.M.M.; Methodology, A.M.M., M.A.M., A.A.A., A.O.D., H.H.A. and R.M.A.Q.; Software, A.M.M., M.A.M., A.A.A., A.O.D., H.H.A. and R.M.A.Q.; Data Curation, M.A.K., N.A.G. and E.M.T.-E.; Writing—Original Draft Preparation, A.M.M. All authors have read and agreed to the published version of the manuscript.

Funding: This research was funded by Deanship of Scientific Research at King Khalid University grant number GRP.1/243/42.

Data Availability Statement: Not applicable.

Acknowledgments: This work was supported by the Deanship of Scientific Research at King Khalid University (Grant number GRP.1/243/42). This paper was also supported by the Engineering Mathematics and Physics Department, Faculty of Engineering and Technology, Future University in Egypt, New Cairo 11845, Egypt. The authors are thankful to Muhammad M Hussain, Integrated Nanotechnology Lab, and Integrated Disruptive Electronic Applications (IDEA) Lab, and Amit Lal, SONIC Lab of Cornell University, for their valuable feedback.

Conflicts of Interest: The authors declare no conflict of interest and no competing financial interests.

References

1. Mayet, A.M.; Hussain, A.M.; Hussain, M.M. Three-terminal nanoelectromechanical switch based on tungsten nitride—An amorphous metallic material. *Nanotechnology* **2015**, *27*, 035202. [[CrossRef](#)]
2. Besozzi, E.; Dellasega, D.; Russo, V.; Conti, C.; Passoni, M.; Beghi, M. Thermomechanical properties of amorphous metallic tungsten-oxygen and tungsten-oxide coatings. *Mater. Des.* **2019**, *165*, 107565. [[CrossRef](#)]
3. Javdošňák, D.; Musil, J.; Soukup, Z.; Haviar, S.; Čerstvý, R.; Houska, J. Tribological properties and oxidation resistance of tungsten and tungsten nitride films at temperatures up to 500 °C. *Tribol. Int.* **2018**, *132*, 211–220. [[CrossRef](#)]

4. Zhao, H.; Ye, F. Effect of Si-incorporation on the structure, mechanical, tribological and corrosion properties of WSiN coatings. *Appl. Surf. Sci.* **2015**, *356*, 958–966. [[CrossRef](#)]
5. Rota, A.; Serpini, E.; Gazzadi, G.C.; Valeri, S. AFM-based tribological study of nanopatterned surfaces: The influence of contact area instabilities. *J. Physics Condens. Matter* **2016**, *28*, 134008. [[CrossRef](#)]
6. Jourshabani, M.; Yun, S.; Asrami, M.R.; Lee, B. Superior photodegradation of organic compounds and H₂O₂ production over tungsten oxide/carbon nitride heterojunction with sizable heptazine units: Dual polycondensation and interface engineering. *Chem. Eng. J.* **2021**, *427*, 131710. [[CrossRef](#)]
7. Paul, D.R.; Gautam, S.; Panchal, P.; Nehra, S.P.; Choudhary, P.; Sharma, A. ZnO-Modified g-C₃N₄: A Potential Photocatalyst for Environmental Application. *ACS Omega* **2020**, *5*, 3828–3838. [[CrossRef](#)]
8. Li, X.; Binnemans, K. Oxidative Dissolution of Metals in Organic Solvents. *Chem. Rev.* **2021**, *121*, 4506–4530. [[CrossRef](#)]
9. Park, W.-P.; Koo, B.-J.; Chang, A.C.; Ferko, T.E.; Parker, J.R.; Ward, T.H.; Lara, S.V.; Nguyen, C.M. Dissolution of Metals from Biosolid-Treated Soils by Organic Acid Mixtures. *Appl. Environ. Soil Sci.* **2016**, *2016*, 9858437. [[CrossRef](#)]
10. Schalenbach, M.; Kasian, O.; Ledendecker, M.; Speck, F.D.; Mingers, A.M.; Mayrhofer, K.J.J.; Cherevko, S. The Electrochemical Dissolution of Noble Metals in Alkaline Media. *Electrocatalysis* **2017**, *9*, 153–161. [[CrossRef](#)]
11. Singh, P.P.; Raja, M.R.K.; Raj, A.; Muqet, M.A. Solution to Interfacing Problems of Programmable Logic Controller in Hardware Replacement. In Proceedings of the 2020 5th IEEE International Conference on Recent Advances and Innovations in Engineering (ICRAIE), Jaipur, India, 1–3 December 2020. [[CrossRef](#)]
12. Rao, D.; Nasir, F.; Department, E. Design of High Gain CMOS Comparator with Slew Rate of 10 V/μs. *IOSR J. VLSI Signal Process.* **2022**, *2*. Available online: <https://www.iosrjournals.org/> (accessed on 16 September 2022).
13. Chen, Z.; Zhu, Z.; Härkönen, K.; Salmi, E. Batch processing of aluminum nitride by atomic layer deposition from AlCl₃ and NH₃. *J. Vac. Sci. Technol. A Vacuum Surfaces Films* **2019**, *37*, 020925. [[CrossRef](#)]
14. Tahir, M.A.R.; Saleem, M.M.; Bukhari, S.A.R.; Hamza, A.; Shakoor, R.I. An efficient design of dual-axis MEMS accelerometer considering microfabrication process limitations and operating environment variations. *Microelectron. Int.* **2021**, *38*, 144–156. [[CrossRef](#)]
15. Moreno, D.; Fan, X.; Niklaus, F.; Villanueva, L.G. Proof of Concept of a Graphene-Based Resonant Accelerometer. In Proceedings of the 2021 IEEE 34th International Conference on Micro Electro Mechanical Systems (MEMS), Gainesville, FL, USA, 25–29 January 2021; pp. 838–840. [[CrossRef](#)]
16. Fan, X.; Forsberg, F.; Smith, A.; Schröder, S.; Wagner, S.; Rödjegård, H.; Fisher, A.; Östling, M.; Lemme, M.; Niklaus, F. Graphene Beams with Suspended Masses as Electromechanical Transducers in Ultra-Small Accelerometers. 2018. Available online: <http://urn.kb.se/resolve?urn=urn:nbn:se:kth:diva-232552> (accessed on 16 September 2022).
17. Fan, X.; Forsberg, F.; Smith, A.D.; Schröder, S.; Wagner, S.; Östling, M.; Lemme, M.C.; Niklaus, F. Suspended Graphene Membranes with Attached Silicon Proof Masses as Piezoresistive Nanoelectromechanical Systems Accelerometers. *Nano Lett.* **2019**, *19*, 6788–6799. [[CrossRef](#)] [[PubMed](#)]
18. Qian, Z.; Rajaram, V.; Kang, S.; Rinaldi, M. High figure-of-merit NEMS thermal detectors based on 50-nm thick AlN nano-plate resonators. *Appl. Phys. Lett.* **2019**, *115*, 261102. [[CrossRef](#)]
19. Ruz, J.J.; Malvar, O.; Gil-Santos, E.; Ramos, D.; Calleja, M.; Tamayo, J. A Review on Theory and Modelling of Nanomechanical Sensors for Biological Applications. *Processes* **2021**, *9*, 164. [[CrossRef](#)]
20. Tapia, J.; Dueñas, A.; Cheje, N.; Soclle, G.; Patiño, N.; Ancalla, W.; Tenorio, S.; Denos, J.; Taco, H.; Cao, W.; et al. Bioleaching of Heavy Metals from Printed Circuit Boards with an Acidophilic Iron-Oxidizing Microbial Consortium in Stirred Tank Reactors. *Bioengineering* **2022**, *9*, 79. [[CrossRef](#)]
21. Rivera, R.M.; Zante, G.; Hartley, J.M.; Ryder, K.S.; Abbott, A.P. Catalytic dissolution of metals from printed circuit boards using a calcium chloride-based deep eutectic solvent. *Green Chem.* **2022**, *24*, 3023–3034. [[CrossRef](#)]
22. Bracamonte, L.; Aulie, V.; Rosenkilde, C.; Einarsrud, K.E.; Sandnes, E. *Dissolution Characteristics and Concentration Measurements of Alumina in Cryolite Melts*; Springer: Berlin/Heidelberg, Germany, 2021; pp. 495–503. [[CrossRef](#)]
23. Shi, K.; Elms, J.; Duan, X.; Poduska, K.M. Droplet asymmetry and wetting dynamics on irregularly roughened surfaces. *J. Coatings Technol. Res.* **2021**, *18*, 911–919. [[CrossRef](#)]
24. Grewal, H.S.; Kim, H.N.; Cho, I.-J.; Yoon, E.-S. Role of Viscous Dissipative Processes on the Wetting of Textured Surfaces. *Sci. Rep.* **2015**, *5*, 14159. [[CrossRef](#)]
25. Grewal, H.S.; Piao, S.; Cho, I.-J.; Jhang, K.-Y.; Yoon, E.-S. Nanotribological and wetting performance of hierarchical patterns. *Soft Matter* **2015**, *12*, 859–866. [[CrossRef](#)] [[PubMed](#)]
26. Shake, R. Chapter 19: A capacitive Accelerometer. In *Microsystem Design*; Springer: Boston, MA, USA, 2002.